Chemical Engineering Journal 445 (2022) 136426

Contents lists available at ScienceDirect

Chemical Engineering Journal

journal homepage: www.elsevier.com/locate/cej

Toward solar-driven photocatalytic CO_2 methanation under continuous flow operation using benchmark MIL-125(Ti)–NH_2 supported ruthenium nanoparticles

María Cabrero-Antonino, Belén Ferrer, Herme G. Baldoví *, Sergio Navalón *

Departamento de Química, Universitat Politècnica de València, Camino de Vera s/n, Valencia 46022, Spain

ARTICLE INFO

Keywords:
Heterogeneous photocatalysis
MIL-125(Ti)–NH_2
Ruthenium nanoparticles
Continuous flow operation
Simulated sunlight irradiation

ABSTRACT

The production of solar fuels from CO_2 is currently attracting increasing interest. Herein we describe the development of a benchmark metal–organic framework (MOF) photocatalyst based on MIL-125(Ti)–NH_2 supported ruthenium nanoparticles for solar-driven selective photocatalytic CO_2 methanation. The optimized RuO_x(10 wt%; 1.48 nm)@MIL-125(Ti)–NH_2 photocatalyst is exceptionally active (18.5 mmol g^{-1} at 22 h) and reusable (10 cycles for 220 h) in the CO_2 methanation at 200 °C under batch conditions and simulated sunlight irradiation. The photocatalyst can also be employed for continuous-flow CO_2 methanation under visible light irradiation at 200 °C for at least 50 h. Evidence in support of the operation of a dual photo-thermal mechanism that combines a photochemical mechanism based on e^-/h^+ separation and thermochemical contributions in which the energy of photons produces local heating has been obtained for the photocatalytic CO_2 methanation. We are confident that this study will contribute to the development of active MOF-based photocatalysts for solar-driven CO_2 methanation under continuous flow operations with industrial interest.

1. Introduction

Fossil fuels now supply about 80% of the worldwide energy demand [1]. As a result of this situation about 70 GTons of CO_2 are emitted into the atmosphere every year, increasing the greenhouse effect, responsible for the global warming and climate change [2–4]. For these reasons there is an urgent need to shift from fossil fuels to renewable energy [5]. In this scenario, recycling CO_2 into fuels and chemicals implementing the first steps for a circular carbon economy is a promising approach towards carbon neutrality [3,5,6]. Regardless the existing large amounts of natural gas resources that contain methane as main product [5], the catalytic CO_2 hydrogenation to CH_4 by using green H_2 in the presence of a catalyst, known as the Sabatier reaction, is one of the most appealing reactions with negative CO_2 footprint for recycling CO_2 on a large scale [7]. Other advantage of the generation of synthetic methane is that can be directly distributed through the existing natural gas infrastructure [5]. Some of the most active catalysts for this process are based on ruthenium species as active sites deposited on a high surface area support, but the reaction still requires high temperatures (T > 300 °C) to achieve high efficiencies [7].

Since the seminal work of Honda and Fujishima, who used TiO_2 as the photoanode for the photocatalytic CO_2 reduction [8], several reports described the use inorganic semiconductor-based materials such as Ru/RuO_x species supported on TiO_2 for the photoreduction of CO_2 to CH_4 by H_2 [9]. More recently, some studies have shown the possibility of performing the solar-driven photoassisted Sabatier reaction at relatively low temperatures (<200 °C). The list of materials employed for this purpose include mostly transition metal oxides such as those based on TiO_2 [10,11] and in less extent carbonaceous materials such as graphene [12–14] or carbon nitride [15], perovskites such as $SrTiO_3$ [16] or $BaTiO_3$ [17] and also metal–organic frameworks (MOFs) [18,19] or MOF-derived materials [20]. In these studies noble-metal ruthenium [10,11,14,16,17] or Pd species have been the preferred co-catalysts while some non-noble metals such as Ni [13,15,19] or Cu [12,18] species have also been employed.

In this context, MOFs [21–25] are considered nowadays as one of the most versatile and tuneable solids with potential for the development of active and efficient photocatalysts [12,13]. Among them, Ti-MOFs gained particular interest as photocatalysts due to their excellent electronic and optical properties, good stability, low toxicity and the abundance of their counterparts [26–29]. The Ti-MOF referred to as MIL-125(Ti)–NH_2 [$(Ti_8O_8)(OH)_4(C_6H_3C_2O_4NH_2)_6$], composed of the 2-

* Corresponding authors.
E-mail addresses: hergarba@qim.upv.es (H.G. Baldoví), sernaol@doctor.upv.es (S. Navalón).

https://doi.org/10.1016/j.cej.2022.136426
Received 15 February 2022; Received in revised form 4 April 2022; Accepted 12 April 2022
Available online 26 April 2022
1385-8947/© 2022 The Author(s). Published by Elsevier B.V. This is an open access article under the CC BY license (http://creativecommons.org/licenses/by/4.0/).

aminoterephthalate organic ligand coordinated to the titanium-oxo cluster, has become one of the benchmark MOF photocatalysts [30], in which the amino group in the terephthalate organic ligand is responsible for absorbing visible light. MIL-125(Ti)–NH_2 exhibits an absorption onset at about 450 nm resulting in an optical band gap of about 2.64 [31]- 2.8 eV [30]. The highest occupied crystal orbital (HOCO) is located at the organic linker, whereas the lowest unoccupied crystal orbital (LUCO) is on the titanium oxo cluster. Theoretical and experimental evidence have confirmed HOCO and LUCO overlapping in MIL-125(Ti)–NH_2, so that irradiating MIL-125(Ti)–NH_2 with appropriate energy leads to a negative ligand-to-metal charge transfer (LMCT) process [32]. In situ electron paramagnetic resonance (EPR) spectroscopy measurements have revealed the formation of photoreduced Ti^{3+} species on irradiating MIL-125(Ti)–NH_2 with UV–Vis light [32,33]. Besides, a common strategy to improve the photoactivity of MOFs is to deposit metal nanoparticles (NPs) within their framework [17,34]. For example, a couple of reports using Cu_2O NPs supported on a Zn-based MOF in 2019 [18] or RuO_x NPs supported on the MIP-208(Ti) in 2020 [17] showed the possibility of using MOF-based photocatalysts for the CO_2 methanation by H_2.

With these precedents in mind, in this work we show the possibility of developing highly active and reusable solar-driven photocatalysts based on the benchmark MIL-125(Ti)–NH_2 solid supported RuO_x NPs for selective CO_2 methanation. The results obtained show that the optimized RuO_x(10 wt%)@MIL-125(Ti)–NH_2 material has the highest reported photocatalytic activity for this process when using MOFs as photocatalysts. In addition the optimized MOF-based photocatalyst prepared in this study can be used for selective CO_2 methanation under continuous flow operation and visible light irradiation. The authors consider that this work will make a significant contribution to the development of MOF-based photocatalysts with outstanding catalytic activity for the production of solar fuels from CO_2.

2. Materials and methods

2.1. Materials

CdSe/ZnS-PEG-COOH-520 were supplied by Hefei Fluonano Biotech. The others reagents employed in this work were of analytical or HPLC grade and supplied by Merck.

2.2. Catalyst preparation

2.2.1. Synthesis of MIL-125(Ti)–NH_2

MIL-125(Ti)–NH_2 was prepared following previously reported procedures [32,35]. 2-aminoterephthalic acid (1.43 g, 7.9 mmol) was dissolved in anhydrous N,N-dimethylformamide (DMF, 20 mL), then, anhydrous methanol (5 mL) was added to the flask and the system sonicated for 20 min. This reaction mixture was transferred to a Teflon-lined autoclave (50 mL), then titanium isopropoxide (1.36 g, 4.8 mmol) was added and the autoclave was sealed and heated up to 110 °C for 72 h. Subsequently, once the system was cooled down to room temperature, the resulting precipitate was filtered, washed with DMF at room temperature for 12 h and, then, washed with DMF at 120 °C for 12 h. This washing procedure was repeated using methanol as solvent. Then, the recovered solid was washed in a Soxhlet for 24 h using methanol as solvent. Finally, the solid was recovered by filtration and dried in an oven at 100 °C.

2.2.2. Preparation of ruthenium nanoparticles on MIL-125(Ti)–NH_2.

Ruthenium was deposited in the previously formed MIL-125(Ti)–NH_2 solid using the photodeposition method [17]. MIL–125(Ti)–NH_2 (50 mg) was dispersed in a mixture of MeOH:Milli-Q water (13:5 mL) using a quartz tube. Then, the corresponding amount of potassium perruthenate previously dissolved in water (2 mL) was added and the system purged with Ar for 20 min. The mixture was irradiated using a UV–vis light lamp during 4 h. The resulting solid was filtered, washed several times with water and dried overnight in an oven at 100 °C.

2.3. Catalyst characterization

Powder X-ray diffractograms (PXRD) were recorded using a Philips XPert diffractometer equipped with a graphite monochromator (40 kV and 45 mA) employing Ni filtered CuK_α radiation. The morphology and composition of the MOF samples were characterized using a scanning electron microscope (SEM, Zeiss instrument, AURIGA Compact) coupled with an energy-dispersive X-ray (EDX) detector. Scanning transmission electron microscopy images in dark field (DF-STEM) were recorded on a JEOL JEM2100F instrument operating at 200 kW. MNP size distribution was estimated by measuring >300 particles from the sample. Isothermal nitrogen adsorption measurements were carried out using an ASAP 2010 Micromeritics device. X-ray photoelectron spectra (XPS) were collected on a SPECS spectrometer with a MCD-9 detector using a monochromatic Al (K_α = 1486.6 eV) X-ray source. Spectra deconvolution was performed after Shirley subtraction of background with the CASA software using the C 1 s peak at 284.4 eV as binding energy reference.

Low temperature CO adsorption on fresh and used RuO_x(10 wt %)/MIL-125(Ti)–NH_2 were investigated by FT-IR spectroscopy by using a Nexus 8700 FTIR spectrophotometer. The IR cell of the instrument allows in situ treatments at controlled temperature and is connected to a high vacuum system with gas dosing facility. Briefly, the sample was pressed into self-supported wafers and treated in vacuum (10^{-6} mbar) at 150 °C for 4 h. Then, the wafers were cooled down to −155 °C under dynamic vacuum followed by CO dosing at increasing pressure (0.4–6 mbar). After each CO dosage the FTIR spectrum was recorded. Temperature-programmed desorption (TPD) coupled to a mass-spectrometer (TPD-MS) analyses of the room temperature equilibrated RuO_x(10 wt%)/MIL-125(Ti)–NH_2 sample (100 mg) were performed in a ChemStar TPx Series (Quantachrome Instruments) instrument connected to a quadrupolar mass-spectrometer. Helium (50 mL/min) was employed as carrier gas and the sample was heated from room temperature to 200 °C at 10 °C min^{-1}.

2.4. Photocatalytic experiments

The photocatalytic CO_2 methanation under batch conditions were carried out using a quartz photoreactor (51 mL) equipped with a heating mantle to control the temperature (Figure S1). Briefly, the powdered photocatalyst (15 mg) previously dried in an oven at 100 °C for 12 h was introduced in the photoreactor, and then the system was purged with H_2 during 20 min and later CO_2 was introduced in the photoreactor until achieving a H_2:CO_2 molar ratio of 4:1 and a final pressure of 1.30 bar. Subsequently, the photoreactor was heated at 200 °C, and then the photocatalyst was irradiated using a commercially available Hg-Xe lamp (150 W, Hamamatsu ref. L8253; Hamamatsu spot light source L9566-04 and light guide A10014-50-0110; Figure S1). To perform the experiments under simulated sunlight irradiation a commercially available AM 1.5G type filter (Lasing ref. 81094) was placed in between the optical fibber and the photoreactor (Figure S1). In some experiments, the influence of the radiation intensity on the photocatalytic reaction was studied by using commercially available transmittance filters (Newport, ref. FSQ-OD30, FSQ-OD15 or FSQ-QD05). In other experiments the optimized RuO_x(10 wt%)/MIL-125(Ti)–NH_2 photocatalyst prepared in this study was activated under Ar flow at different temperatures (100, 175, 190 and 200 °C) for 20 min before the H_2 and CO_2 are introduced in the system as described above. The photocatalytic CO_2 methanation under continuous flow operation was carried out using a cylindrical quartz column (length 26 cm, diameter 1.2 cm) were the catalyst pellets (50 mg; catalyst pellet size 0.2 μm) is placed in the middle of the column (Figure S1). The system is equipped with a heating mantle to control the temperature (150 or 200 °C). The photocatalyst is irradiated with visible light (150 W Hg-Xe lamp equipped with a filter of cut-off λ > 420 nm

Newport filter ref FSQ-GG420 installed in the Hamamatsu filter holder) using a guide light optical fibber (Figure S1). It should be commented that the commercially available AM 1.5 G type filter available in our laboratory is not compatible with the Hamamatsu filter holder and due to the photocatalytic setup shown in Figure S1 cannot be placed in between the photocatalyst and the optical fibber during the continuous flow experiments. A mass flow controller was employed to feed the mixture of gases (H_2 80% and CO_2 20%) at 20 mL/min. At the desired reaction time, an aliquot was sampled from the batch or continuous flow photoreactor and analysed in an Agilent 490 MicroGC equipped with two channels and thermal conductivity detectors. One channel equipped with a MolSieve 5A° column allowed the analysis of H_2, O_2, N_2, and CO, whereas the other channel equipped with a Pore Plot Q column allowed the determination of CO_2, CH_4, and short-chain hydrocarbons. Quantification was performed using calibration plots employing commercially available gas mixtures.

2.5. Photocurrent measurements

Photocurrent measurements were carried out in a standard three-electrode electrochemical cell using a transparent fluoride-doped tin oxide (FTO)-coated glass substrate on which a thin layer of the corresponding fresh or used RuO_x(10 wt%)@MIL–125(Ti)–NH_2 sample was deposited (FTO-RuO_x(10 wt%)@MIL-125(Ti)–NH_2). The FTO-RuO_x(10 wt%)@MIL-125(Ti)–NH_2 films were employed as working electrode, a platinum wire as the counter electrode and a standard calomel electrode (SCE) as the reference electrode. The oxygen present in the cell was removed purging the electrolyte with Ar for 20 min. The photocurrent was measured under dark and under illumination polarizing the working electrode at potentials from 1.4 to 0.2 V. Irradiations were performed using an optical fibber connected to a 150 W Hg-Xe lamp equipped with an AM 1.5G type filter.

2.6. Photoluminiscence experiments

Photoluminescence (PL) spectroscopy measurements were carried out with JASCO FP-8500 instrument. Measurements using RuO_x(10 wt %)/MIL–125(Ti)–NH_2 or MIL–125(Ti)–NH_2 took place after adjusting absorption of the samples to 0.35 a.u. at 340 nm (the excitation wavelength) in acetonitrile after purging the quartz cuvette with Ar to remove oxygen from suspension. Relative quantum efficiency was calculated dividing fluorescence curve area of fresh or used RuO_x(10 wt %)/MIL–125(Ti)–NH_2 by that obtained using MIL–125(Ti)–NH_2.

PLs measurements were also performed using commercially available and water dispersible CdSe-ZnS core–shell quantum dots (QDs, 304-CdSe/ZnS-PEG-COOH-520) supported on a quartz glass plate. Previously, an acetonitrile solution of CdS-ZnS QDs was dropwise with a pipette on a quartz glass plate. Subsequently the system was dried at 50 °C using a laboratory hot plate. Before the PL measurements the supported CdSe-ZnS QDs on the quartz glass plate was heated on a laboratory hot plate at the required temperature before and after irradiation the system with a Xe-Hg lamp (150 W) for 20 min. Similar measurements were carried out using CdSe-ZnS QDs supported on RuO_x(10 wt%)/MIL-125(Ti)–NH_2. Previously, RuO_x(10 wt%)/MIL-125 (Ti)–NH_2 was supported on a quartz glass plate by using the doctor blade technique using a suspension of the material in terpineol and acetone. Then, an acetonitrile solution of CdSe-ZnS QDs was dropwise on the quartz glass plate containing the RuO_x(10 wt%)/MIL-125(Ti)–NH_2 sample.

3. Results and discussion

In this study we aimed to develop a highly active photocatalyst for solar-driven CO_2 methanation based on the benchmark MIL-125(Ti)–NH_2 solid supported ruthenium NPs. For this, a series of MIL-125(Ti)–NH_2 with increasing loadings of RuO_x NPs were prepared and characterized. The photocatalytic activity of the MOF-based photocatalysts was then tested for CO_2 methanation under batch and continuous flow operations under simulated sunlight and visible light irradiation, respectively. The stability and reusability of the most active photocatalyst were assessed under both batch and continuous flow operations. Additional photocatalytic experiments and spectroscopic measurements were performed to gain insights into the photocatalytic methanation mechanism with the most active sample.

3.1. Photocatalyst preparation

In the first step the benchmark MIL-125(Ti)–NH_2 was prepared according previous reports [17], after which a series of ruthenium NP co-catalysts at different loadings supported MIL-125(Ti)–NH_2 were prepared by the photodeposition method. The XRD patterns of MIL-125 (Ti)–NH_2 solid with or without ruthenium NPs matched well with its simulated diffraction pattern, while the PXRD of MIL-125(Ti)–NH_2 supported ruthenium NPs also presented a diffraction peak characteristic of the RuO_2 (1 1 0) facet (Fig. 1).

HRSEM images of pristine MIL-125(Ti)–NH_2 sample revealed its characteristic circular plate-like morphology was maintained after loading the RuO_x NPs in the MOF (Fig. 2a,b and Figure S2). EDX analyses of the samples confirmed that the initial amounts of ruthenium (from 1 to 10 wt%) were photodeposited within the MIL-125(Ti)–NH_2 solids. Attempts to further increase the ruthenium loading by using an initial amount of 20 wt% produced a sample with a content of 11.5 wt% as revealed by EDX, so that we focused on the MIL-125(Ti)–NH_2 samples with ruthenium loadings from 1 to 10 wt%. The EDX elemental map of the series of the samples revealed good dispersion of ruthenium in the MIL-125(Ti)–NH_2 support (Fig. 2c and Figures S3-S7).

Interestingly, DF-STEM measurements of the RuO_x loaded MIL-125 (Ti)–NH_2 samples estimated a similar small ruthenium particle size distribution in all the samples (Figure S8). In these cases the EDX detector coupled to DF-STEM was used to confirm the presence of ruthenium in the NPs dispersed on the MIL-125(Ti)–NH_2 support (Figures S9 to S12).

The porosity of the samples was evaluated by isothermal nitrogen adsorption experiments (Figure S13). The pristine MIL-125(Ti)–NH_2 had a BET surface area and pore volume of 1214 m^2/g and 0.57 cm^3/g, in good agreement with previous reports [31]. As expected, RuO_x deposition within the MOF network at increasing loadings gradually reduced both BET and pore volume. It should be noted that the RuO_x/MIL-125 (Ti)–NH_2 samples with RuO_x loadings of 1 (1,041 m^2/g; 0.47 cm^3/g), 2 (1,021 m^2/g; 0.47 cm^3/g), 5 (1,000 m^2/g; 0.46 cm^3/g), and even those at 10 (770 m^2/g; 0.33 cm^3/g) wt% loading still had relatively high porosity.

The optical absorption properties of the MIL-125(Ti)–NH_2 samples under study with or without RuO_x NPs were inspected by UV–Vis diffuse reflectance spectroscopy (Fig. 3a). The UV–Vis MIL-125(Ti)–NH_2 spectrum was characterized by one band centred at 280 nm associated with the O to Ti ligand-to-metal charge transfer, together with a band centred at 380 nm attributable to the charge transfer from the 2-aminoterephthalate ligand to the $Ti_8O_8(OH)_4$ cluster [36]. The band gap of pristine MIL-125(Ti)–NH_2 estimated from the Tauc plot was 2.74 eV, in good agreement with previous reports [30,31]. The deposition of RuO_x NPs within the MIL-125(Ti)–NH_2 material increased the absorption band beyond 800 nm with respect to pristine MIL-125(Ti)–NH_2 solid due to the RuO_x plasmon band (Fig. 3b) [37].

XPS was also employed for the characterization of the most active sample of the series during photocatalytic CO_2 reduction, which was RuO_x@(10 wt%)@MIL-125(Ti)–NH_2 (Fig. 4). XPS spectra of C 1 s and Ru 3d confirmed the presence of aromatic carbons (284.4 eV) together with the characteristic signals of carbon atoms bonded to the amino group (C-N, 285.9 eV) and in the carboxylate functional groups (288.6 eV) [31]. The Ru 3d3/2 XPS signal partially overlapped the C 1s spectrum. The band centred at about 281.7 eV can be attributed to the presence of

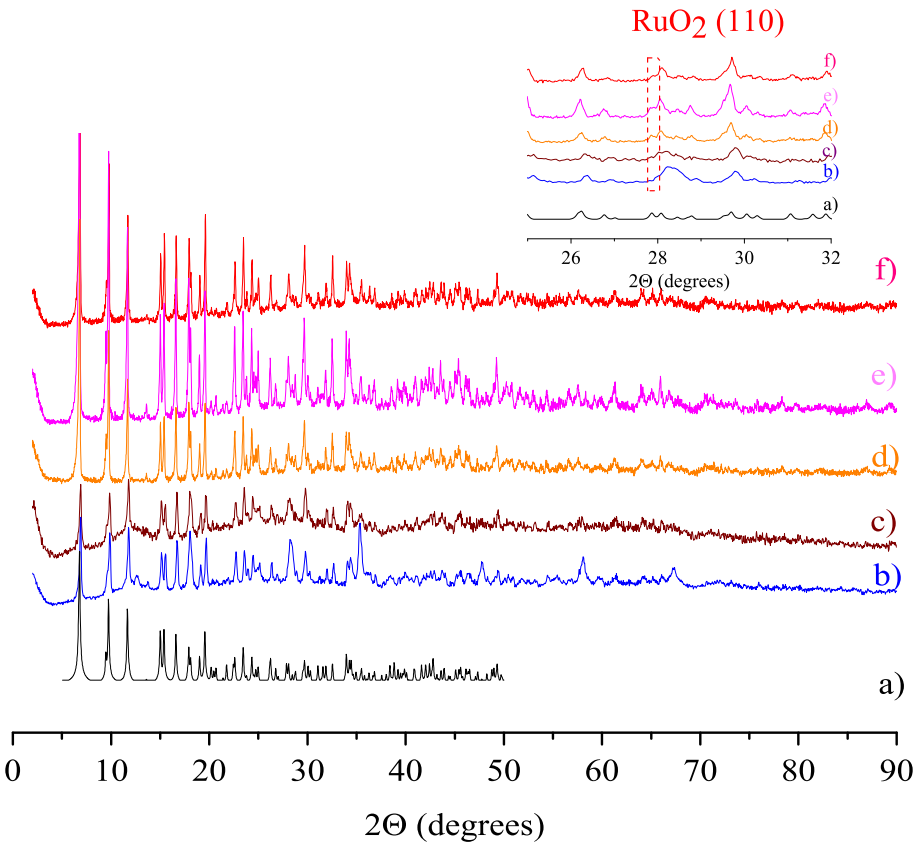

Fig. 1. PXRD of simulated MIL-125(Ti)–NH_2 (a), pristine MIL-125(Ti)–NH_2 (b), RuO_x(1 wt%)MIL-125(Ti)–NH_2 (c), RuO_x(2 wt%)MIL-125(Ti)–NH_2 (d), RuO_x(5 wt%) MIL-125(Ti)–NH_2 (e), RuO_x(10 wt%)MIL-125(Ti)–NH_2 (f). The inset shows a zoom-in of the characteristic RuO_2 (1 1 0) facet.

RuO_2 and hydrated ruthenium species [38,39]. The other expected Ru 3d3/2 shifted 4.17 eV, however it overlapped the C-N band [39,40]. The broad O 1 s XPS band was centred at about 532 eV due to the presence of oxygen atoms in the carboxylate groups (~530.5 eV) together with the Ti-O and Ru-O bonds (<530.5 eV). XPS spectra of Ti 2p and Ru 3p XPS mainly attributable to the presence of Ti^{4+} ions of the Ti-oxo cluster (Ti 2p3/2 458.8 eV and Ti 2p1/2 at 464.3 eV) [31] together with RuO_2 NPs (Ru 3p3/2 at 462.6 eV and Ru 3p1/2 at 485.6 eV) [41]. Previous reports have shown that the N 1s XPS of MIL-125(Ti)–NH_2 is composed of a main band centred at about 399 eV and another smaller band at 401 eV due to the presence of free and partially protonated amino groups, respectively [31]. The N 1 s XPS of RuO_x@(10 wt%)@MIL-125(Ti)–NH_2 sample showed similar XPS bands to the MOF pattern but shifted about 2 eV to higher binding energies. This observation can be attributed to a good interaction between the RuO_x NPs and the amino groups present in the MOF network. This interaction between RuO_x NPs and the amino groups present in the MOF can be at least partially responsible for the small RuO_x particle size distribution obtained in all the samples, even at loadings as high as 10 wt%. It should be noted that in the field of supported NPs the particle size distribution of the NPs is generally seen to increase with the metal loading in a heterogeneous support, due to the coverage of anchoring sites in the support [42,43]. Other examples have also shown that the presence of amino groups in MOFs' organic ligands favour the deposition of small MNPs and avoid metal NP agglomeration during catalytic processes [44].

3.2. Photocatalytic activity

3.2.1. Photocatalytic CO_2 methanation under batch conditions

The photocatalytic activity of MIL-125(Ti)–NH_2 supported RuO_x NPs at different metal loadings was initially evaluated for CO_2 methanation at 200 °C under simulated sunlight irradiation. Control experiments showed that the reaction did not occur in the absence of a photocatalyst under the reaction conditions studied. The use of MIL-125(Ti)–NH_2 as photocatalyst in the absence of RuO_x as co-catalyst resulted in low CO_2 methanation production (~15 μmol g^{-1} after 22 h). In contrast, RuO_x NPs supported on MIL-125(Ti)–NH_2 promoted the selective photocatalytic CO_2 methanation under simulated sunlight irradiation (Fig. 5a). The use of only 1 wt% of RuO_x NPs supported on MIL-125(Ti)–NH_2 resulted in a CO_2 conversion of 2.8% and a CH_4 production of 924 μmol g^{-1} after 22 h. To put this value in context, this photocatalytic activity was compared with that observed in some related reports using MOF-based photocatalysts. In 2019 it was reported that Cu_2O (1 wt%) supported on a Zn-based MOF exhibits a CH_4 production of 45 μmol g^{-1} at 215 °C under UV–Vis irradiation after 24 h [18]. More recently, some of us reported that RuO_x NPs (1 wt%) supported on a Ti-based MOF namely MIP-208 is an active photocatalyst for the CO_2 methanation (700 μmol CH_4 g^{-1} after 22 h) under simulated sunlight irradiation [17]. Therefore, the photoactivity of RuO_x(1 wt%)@MIL-125(Ti)–NH_2 compares favorably to the previous analogous reports.

Fig. 5 also shows that using the same amount of photocatalyst, there was a positive linear relationship between increasing the ruthenium content in MIL-125(Ti)–NH_2 for both photocatalytic CO_2 conversion and CH_4 production (μmol g^{-1} catalyst h^{-1}). The RuO_x(10 wt%)@MIL-125 (Ti)–NH_2 sample having the highest RuO_x loading resulted in the most active photocatalyst in terms of CO_2 both conversion (52%) and CH_4 production (18.5 mmol g^{-1} after 22 h). For this reason the RuO_x(10 wt %)@MIL125(Ti)–NH_2 photocatalyst was selected as the optimized photocatalyst for both batch and flow operations. A control experiment using the RuO_x(10 wt%)@MIL125(Ti)–NH_2 solid catalyst in the presence of H_2 at 200 °C under dark conditions gave a CO_2 conversion (20% at 22 h) and CH_4 production (7 mmol g^{-1} at 21 h) of about 38% of the same experiment under simulated sunlight irradiation. The fact that the catalyst showed activity in the dark was not unexpected, since, as

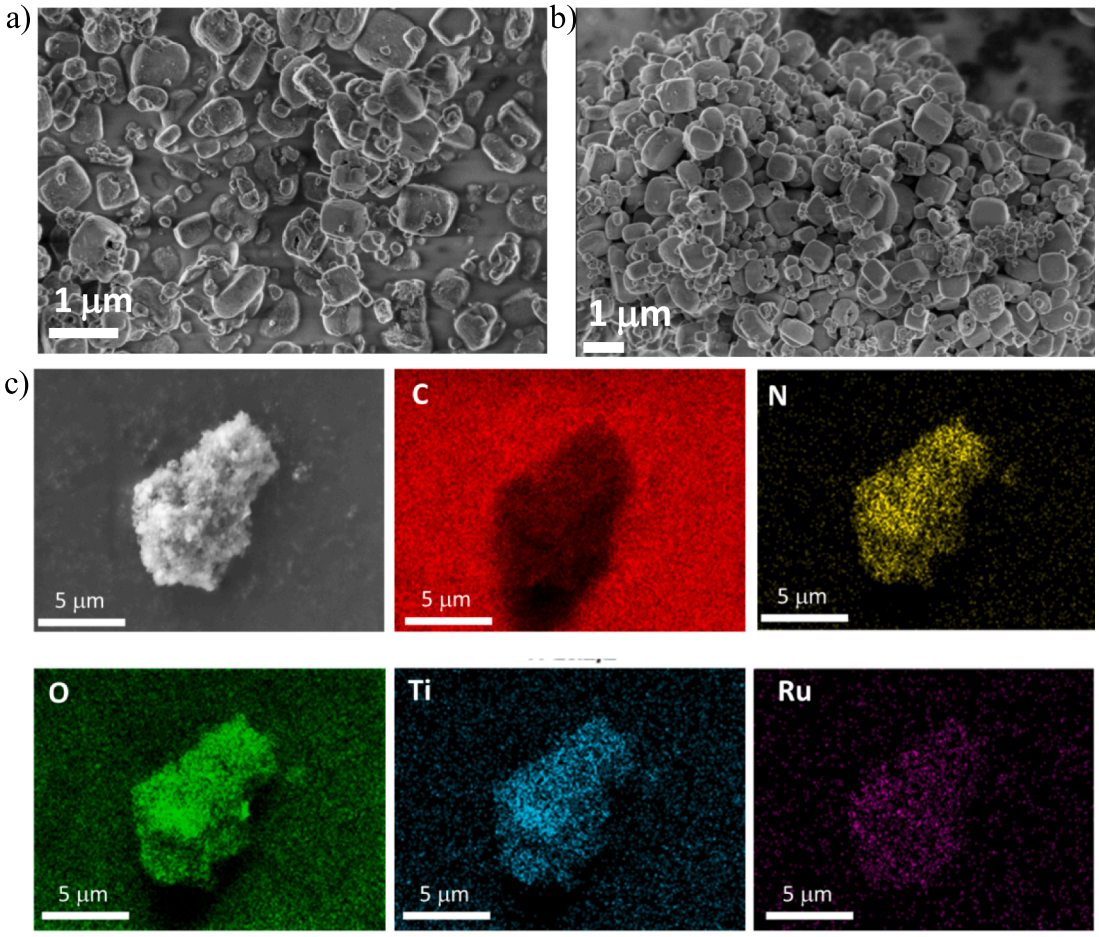

Fig. 2. HRSEM image of MIL-125(Ti)–NH_2 (a) and RuO_x(10 wt%)@MIL-125(Ti)–NH_2 (b). SEM image and EDX mapping of RuO_x(10 wt%)@MIL-125(Ti)–NH_2 (c)

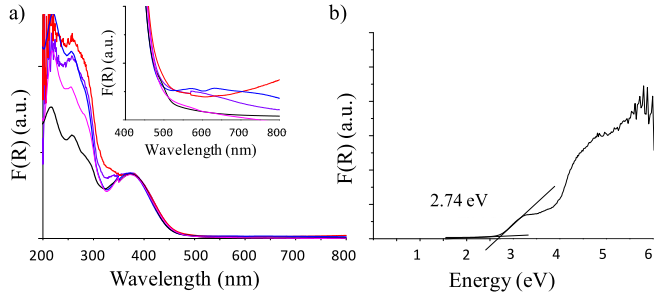

Fig. 3. a) Diffuse reflectance UV–Vis spectra of MIL-125(Ti)–NH_2 (black line), RuO_x(1 wt%)MIL-125(Ti)–NH_2 (pink line), RuO_x(2 wt%)MIL-125(Ti)–NH_2 (purple line), RuO_x(5 wt%)MIL-125(Ti)–NH_2 (blue line), RuO_x(10 wt%)MIL-125(Ti)–NH_2 (red line). The inset shows a zoom-in of the region between 400 and 800 nm. b) Tauc plot of pristine MIL-125(Ti)–NH_2 sample.

commented above, ruthenium-based NPs are some of the most active species in CO_2 hydrogenation [7]. As it will be shown later, experimental evidences of the occurrence of a dual photo-thermal mechanism using the most active RuO_x(10 wt%)@MIL125(Ti)–NH_2 photocatalyst have been obtained.

One of the significant features of RuO_x(10 wt%)@MIL-125(Ti)–NH_2 as photocatalyst is its high selectivity towards reducing CO_2 to CH_4 (Fig. 6). Other possible reaction products such as CO of higher chain hydrocarbons have not been observed under the present reaction conditions. Some studies have pointed out that selective CO_2 hydrogenation to CH_4 or CO can be explained by the adsorption strength of CO as reaction intermediate close to the hydrogenation active centres of the photocatalyst [45]. Strong adsorption of CO to the active centres further reduces this intermediate to CO, while CO is the main reaction product when this molecule has a low affinity for binding to the active centres. A series of in situ FT-IR measurements were performed using CO as probe molecule to evaluate possible reasons for the high selectivity of RuO_x(10 wt%)@MIL-125(Ti)–NH_2 as photocatalyst for CH_4. Fig. 6 shows the in situ CO adsorption on solid MIL-125(Ti)–NH_2. The band appearing at about 2138 cm^{-1} can be assigned to physisorbed CO within the MOF that disappears upon evacuation [46,47]. This observation was not unexpected, due to the absence of coordinatively unsaturated Ti^{4+} ions in the MIL-125(Ti)–NH_2 material. Using RuO_x(10 wt%)@MIL-125(Ti)–NH_2 material also exhibits a broad band centred at 1972 cm^{-1} together with a shoulder at 2058 cm^{-1} characteristic of chemisorbed CO into RuO_x [48]. Due to CO chemisorption into RuO_x NPs present in the MIL-125(Ti)–NH_2, the evacuation process under vacuum does not significantly reduce the chemisorbed CO band intensity of the in situ FT-IR while negligible physisorbed CO signals can be now observed. These results are in agreement with the ability of RuO_x(10 wt%)@MIL-125(Ti)–NH_2 as photocatalyst for selective CO_2 methanation. As it will be shown latter (section 2.2.2) the used RuO_x(10 wt%)@MIL-125(Ti)–NH_2 sample at 200 °C during the photocatalytic CO_2 methanation with H_2 is characterized by a partial reduction of RuO_x NPs as evidenced by PXRD and XPS measurements. Regardless these comments, in situ CO adsorption on the used RuO_x(10 wt%)@MIL-125(Ti)–NH_2 catalyst also shows the presence of the bands at about 2058 and 1972 cm^{-1} even after evacuation under vacuum indicating the ability of these partially reduced RuO_x NPs to chemisorb CO (Figure S14) [49].

To confirm that RuO_x(10 wt%)@MIL-125(Ti)–NH_2 could

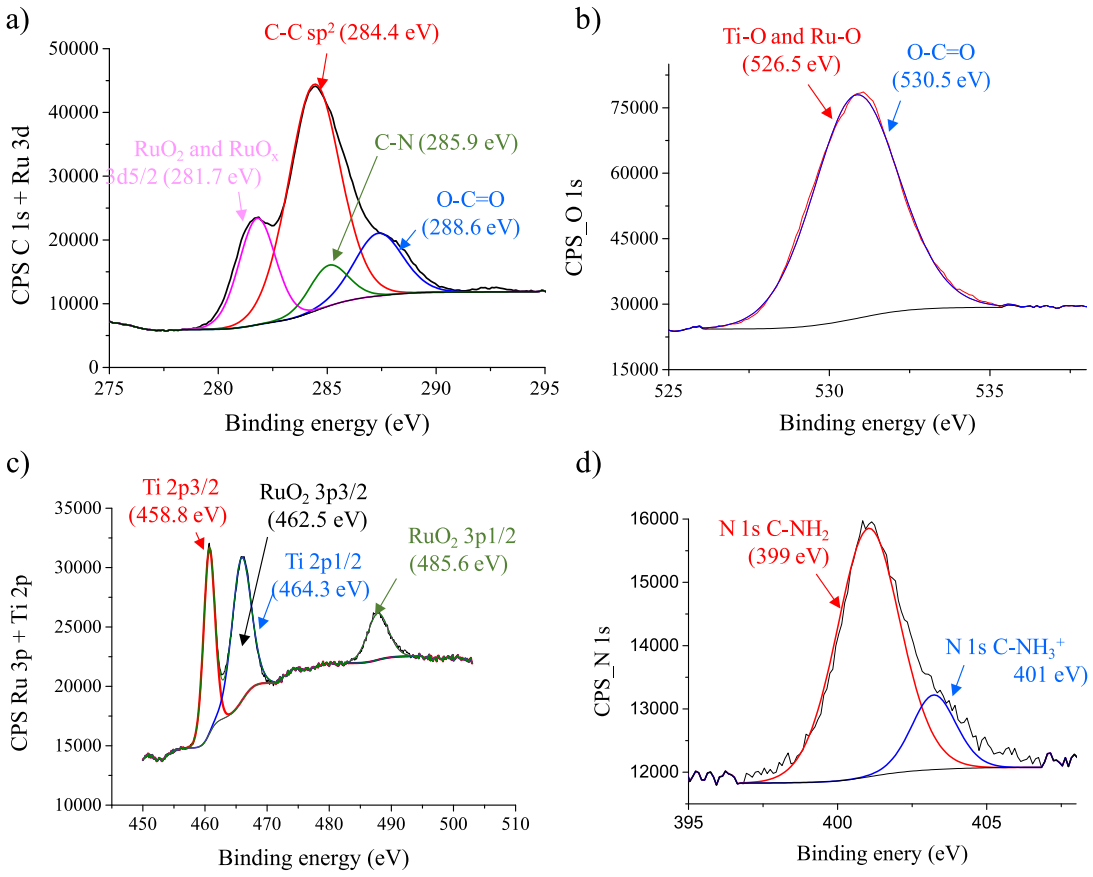

Fig. 4. XPS C 1 s + Ru 3d (a), O 1s (b), Ti 2p + Ru 3p (c) and N 1s (d) of the RuO_x(10 wt%)@MIL-125(Ti)–NH_2 solid.

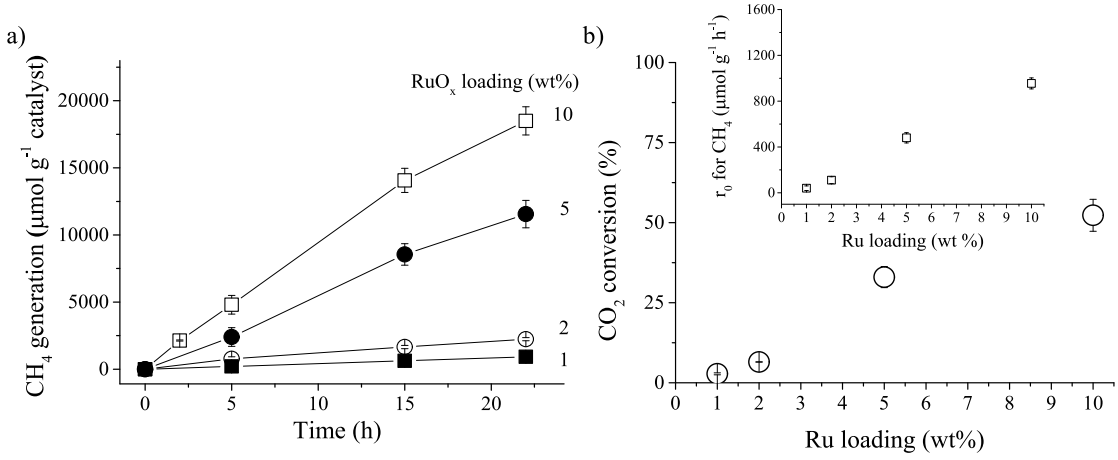

Fig. 5. a) Photocatalytic CH_4 production using different loadings of RuO_x NPs supported on MIL-125(Ti)–NH_2 under simulated sunlight irradiation. Legend: 1 (■), 2 (○), 5 (●) and 10 (□) wt%. b) Influence of simulated sunlight irradiation on CO_2 photoreduction to CH_4 using RuO_x(10 wt%)@MIL-125(Ti)–NH_2. Reaction conditions: Photocatalyst (15 mg), P_{H2} = 1.05 bar, P_{CO2} = 0.25 bar, reaction temperature (200 °C), simulated sunlight irradiation (Hg-Xe lamp of 150 W equipped with an AM 1.5G type filter).

photocatalytically convert CO_2 to CH_4 (Eq.1), some experiments were performed using isotopically labelled $^{13}C^{18}O_2$ during the photocatalytic reaction. Analysis of the gas phase by mass spectrometry after 22 h of photocatalytic reaction revealed the formation of $^{13}CH_4$ (*m/z* 17) together with $H_2^{18}O$ (*m/z* 20) (Figure S15). The simultaneous presence of $^{13}CH_4$ and $H_2^{18}O$ was attributed to the system's low separation efficiency for these two compounds. It should be noted that $^{13}CH_4$ and $H_2^{18}O$ were not present in the gas phase of the reaction system at time 0 before irradiation.

$$CO_2 + 4\ H_2 \rightarrow CH_4 + 2\ H_2O \quad (1)$$

The influence of the reaction temperature on the photocatalytic CO_2 methanation using the optimized RuO_x(10 wt%)@MIL125(Ti)–NH_2 material was studied (Fig. 7). It is important to note that the possibility of developing solar-driven heterogeneous photocatalytic systems for CO_2 methanation at relatively low reaction temperatures is important as regards both technology and economy. The obtained results indicate

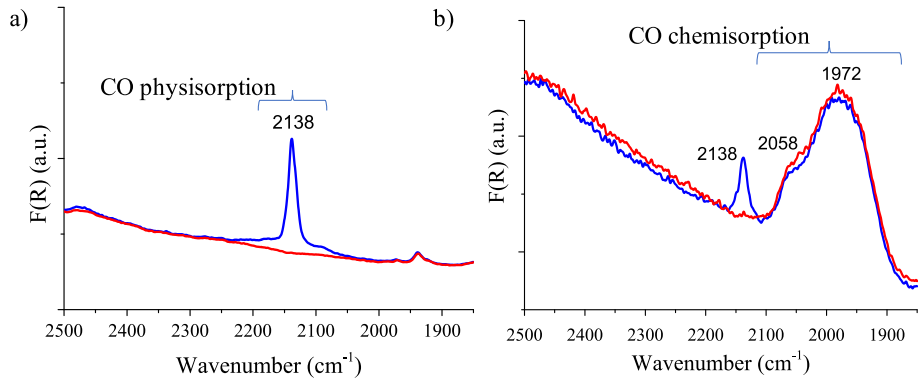

Fig. 6. FT-IR spectra of CO adsorbed in MIL-125(Ti)–NH_2 (a) or RuO_x(10 wt%)@MIL-125(Ti)–NH_2 at −155 °C. Blue lines indicate the CO uptake at saturation by MIL-125(Ti)–NH_2 (a) or RuO_x(10 wt%)@MIL-125(Ti)–NH_2 (b) materials. Red lines indicate desorption of CO under vacuum from the solids after achieving their maximum CO uptake.

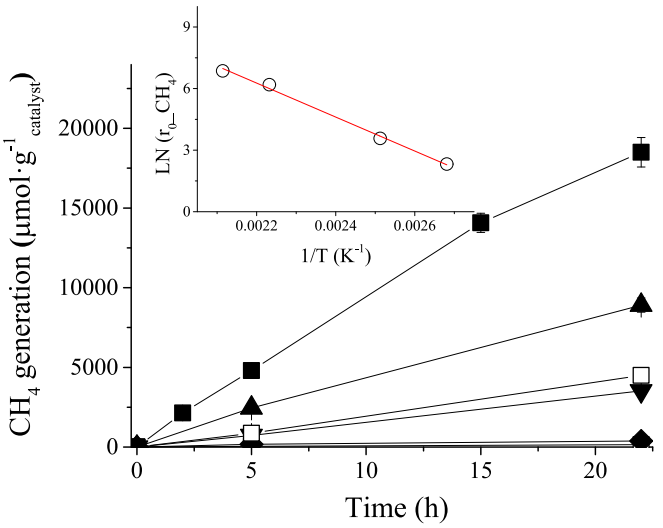

Fig. 7. Photocatalytic CO_2 methanation using RuO_x(10 wt%)@MIL-125(Ti)–NH_2 as a function of the reaction temperature. Legend: 200 °C (■), 175 °C (▲), 165 °C (▼), 125 °C (◆); 200 °C in the presence of H_2O (60 μL, □). The inset shows the Arrhenius plot of CH_4 generation as a function of the reaction temperature. Reaction conditions: Photocatalyst (15 mg), P_{H2} = 1.05 bar, P_{CO2} = 0.25 bar, simulated sunlight irradiation (Hg-Xe lamp of 150 W equipped with an AM 1.5G type filter), reaction temperature as indicated.

that the photocatalytic CO_2 methanation using the most active RuO_x(10 wt%)@MIL125(Ti)–NH_2 sample under constant simulated sunlight irradiation increased exponentially with temperature, according to the Arrhenius equation. The apparent activation energy for CO_2 methanation by RuO_x(10 wt%)@MIL125(Ti)–NH_2 was estimated to be 68.8 kJ mol^{-1}. This observation suggests that the photocatalytic process can be also activated by temperature. In fact, as it will be shown later experimental evidences using the RuO_x(10 wt%)@MIL125(Ti)–NH_2 photocatalyst suggest the occurrence of a dual photo-thermal reaction mechanism that combines a photochemical mechanism based on electron/hole separation together with a thermochemical pathway in which the energy of photons produces local heating that promotes the photocatalytic reaction.

To gain information about the thermal activation required when using RuO_x(10 wt%)@MIL125(Ti)–NH_2 as photocatalyst for CO_2 methanation some control experiments were carried out·H_2O was formed during photocatalytic CO_2 hydrogenation reaction (Eq. (1)) and could be adsorbed on the MOF and interact with the active sites in the photocatalyst. In order to validate this hypothesis, a control photocatalytic reaction was carried out using solid RuO_x(10 wt%)@MIL-125(Ti)–NH_2 at 200 °C under simulated sunlight irradiation in the presence of water. As the photocatalytic activity of RuO_x(10 wt%)@MIL-125(Ti)–NH_2 (18.5 mmol g^{-1} after 22 h) is reduced (~4.5 mmol g^{-1} after 22 h) in the presence of water (60 μL; Fig. 8), it can be supposed that the photocatalytic activity of RuO_x(1 wt%)@MIL-125(Ti)–NH_2 at reaction temperatures higher than 175 °C should favour water desorption from the active centres of the photocatalysts and thus enhanced activity. In fact, the water desorption as a function of the temperature from the room temperature equilibrated RuO_x(1 wt%)@MIL-125(Ti)–NH_2 sample was confirmed by TPD-MS analysis. Figure S16a shows that water desorption upon relevant photocataytic conditions in this study from the RuO_x(1 wt%)@MIL-125(Ti)–NH_2 solid mostly occurs in the range from 30 to 175 °C and in less extent at temperatures in between 175 and 200 °C. Furthermore, additional photocatalytic experiments on CO_2 reduction by H_2 at 200 °C using the RuO_x(1 wt%)@MIL-125(Ti)–NH_2 sample activated under argon flow at 100, 175, 190 and 200 °C for 20 min clearly shows that activation at temperatures above 190 °C favors the photocatalytic activity (Figure S16b). In conclusion, TPD-MS data and the influence of RuO_x(10 wt%)@MIL-125(Ti)–NH_2 thermal activation before its use as photocatalyst revealed that the removal of adsorbed water from the solid favors the resulting photocatalytic activity.

3.2.2. *Photocatalyst stability under batch and continuous flow operations*

Photocatalytic stability and reusability are basic requisites for the development of industrial processes. MOFs' main limitations include thermal, chemical and photochemical stability for use as photocatalysts and deserve especial attention [26,30,50]. The photocatalytic activity and stability of RuO_x(10 wt%)@MIL-125(Ti)–NH_2 were first evaluated under batch reaction conditions with simulated sunlight irradiation at 200 °C. Fig. 8a shows that the photocatalyst retained its activity for 220 h during CO_2 methanation in ten consecutive reuses. PXRD shows that the MOFs' crystallinity was also retained at least for ten cycles (220 h) during the reuse experiments (Fig. 8b) and also that the initial RuO_2 NPs supported on the RuO_x(10 wt%)@MIL-125(Ti)–NH_2 photocatalyst were mostly transformed into reduced Ru NPs after the first use (Fig. 8b). To gain more information about the oxidation state of ruthenium present in the used RuO_x(10 wt%)@MIL-125(Ti)–NH_2 sample a XPS analysis was carried out (Figure S17). The Ru 3d XPS spectrum of the used photocatalyst shows two bands centered at 279.4 and 281 eV attributable to the presence of metallic Ru^0 and partially reduced RuO_x NPs, respectively. The presence of the new Ru 3d XPS band at lower binding energy in the used photocatalyst (279.5 eV) respect to the fresh one, characterized by a Ru 3d band centered at 281.7 eV, confirms a partial reduction of RuO_2 to Ru^0 and RuO_x during the photocatalytic process [51]. In good agreement with these observations, the Ru 3p XPS of the used photocatalyst shows a significant reduction of the band at 484.4 eV and at about 462.6 eV both characteristic of the presence of RuO_2 NPs in

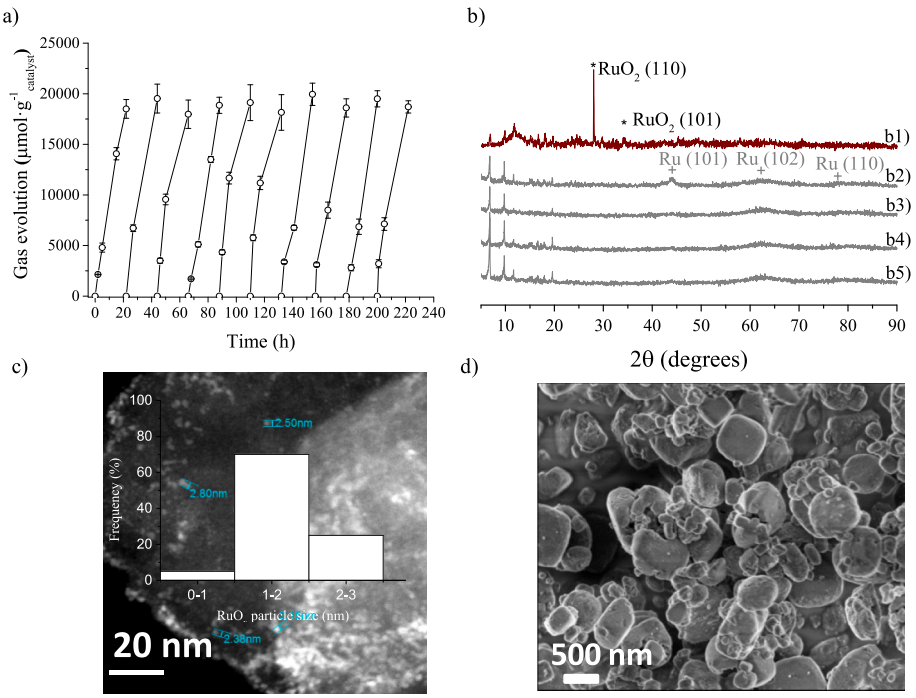

Fig. 8. a) RuO_x(10 wt%)@MIL-125(Ti)–NH_2 reusability during CO_2 methanation under batch operation. Reaction conditions: Photocatalyst (15 mg), P_{H2} = 1.05 bar, P_{CO2} = 0.25 bar, reaction temperature (200 °C), simulated sunlight irradiation (Hg-Xe lamp of 150 W equipped with an AM 1.5G filter). b) PXRD of the fresh- (a), one-time (b), four-times (c), six-times (d) and seven-times (e) used photocatalyst. c) DF-TEM image and RuO_x particle size distribution of the photocatalyst after being used seven times. d) SEM image of the seven-times used photocatalyst.

the fresh RuO_x(10 wt%)@MIL-125(Ti)–NH_2 sample (Fig. 4).

TEM measurements of the RuO_x(10 wt%)@MIL-125(Ti)–NH_2 photocatalyst after seven cycles showed that the ruthenium particle size distribution had been maintained (Fig. 8c and S18). The previously commented strong interaction observed by XPS between ruthenium NPs and the NH_2 groups present in the RuO_x(10 wt%)@MIL-125(Ti)–NH_2 could at least be responsible for the negligible ruthenium NPs aggregation during the photocatalytic tests at 200 °C, even after 154 h. SEM measurements also confirmed that the sample retained its morphology after reuse (Fig. 8d). RuO_x(10 wt%)@MIL-125(Ti)–NH_2 had good overall stability after reuse. It should be noted, however, that some authors had previously reported that carboxylate-based MOFs suffer partial decarboxylation under long-term (weeks) UV–Vis irradiation at 200 °C [50]. In this work, a control experiment with RuO_x(10 wt%)@MIL-125(Ti)–NH_2 in an Ar atmosphere and simulated light irradiation for 22 h showed a partial decarboxylation of about 2.1 mol% of the initial MOF ligand.

To put into context the obtained results, the photocatalytic activity and stability of RuO_x(10 wt%)/MIL-125(Ti)–NH_2 sample was compared with analogous previous reports (Table S1). From this table it can be concluded that the photocatalytic activity (0.84 mmol $g^{-1}h^{-1}$) and stability (220 h operation during 10 consecutive cycles) under simulated sunlight irradiation ranks RuO_x(10 wt%)/MIL-125(Ti)–NH_2 among the most active MOF-based materials reported until now for photocatalytic CO_2 methanation. Comparison with other heterogeneous photocatalysts based on transition metal oxides, carbonaceous materials or MOF-derived materials is more cumbersome and it should be taken cautiously due to the variability in the employed reaction conditions (irradiation source, light intensity, catalyst amount, co-catalyst amount, photoreactor design), particularly because the so-far reported photocatalysts were not reused or, having an apparent higher activity of the fresh material, it deactivated upon reuse, something that has not been observed in the present case. Regardless the exact ranking of RuO_x(10 wt%)/MIL-125(Ti)–NH_2, it is clear that the photocatalytic stability of the optimized RuO_x(10 wt%)/MIL-125(Ti)–NH_2 sample prepared in our study compares very favourably with previous reports using other heterogeneous-based photocatalysts with the additional advantage of being easily tuneable to increase further the activity.

As commented in the introduction, the industrial generation of solar fuels requires the development of continuous flow processes. Due to the high photocatalytic activity and good stability of RuO_x(10 wt%)@MIL-125(Ti)–NH_2 under batch conditions we decided to perform photocatalytic methanation in a continuous flow operation under visible light irradiation ($\lambda > 420$ nm). Fig. 9a shows that the RuO_x(10 wt%)@MIL-125(Ti)–NH_2 photocatalyst can operate efficiently at least 50 h under continuous flow at 150 or 200 °C under visible light irradiation with only 3 s of contact time. The crystallinity of the RuO_x(10 wt%)@MIL-125(Ti)–NH_2 photocatalyst used was maintained after 40 h of operation, as revealed by PXRD measurements (Fig. 9b). As in batch conditions, the oxidation state of supported RuO_x NPs in the fresh MIL-125(Ti)–NH_2 photocatalyst changes to Ru^0, while TEM (Fig. 9c and Figure S19) and SEM (Fig. 9d) measurements show that the ruthenium particle size distribution and morphology of the RuO_x(10 wt%)@MIL-125(Ti)–NH_2 sample used under continuous flow operation were maintained, respectively.

3.2.3. *Reaction mechanism*

There are in the literature several examples describing the use of MIL-125(Ti)–NH_2 as photocatalyst operating under a pure photochemical mechanism [24,32]. The generally accepted reaction mechanism using MIL-125(Ti)–NH_2 upon photoexcitation with appropriate energy results in an LMCT process [32]. Other reports have also reported that the use of Ru and/or RuO_x NPs as co-catalyst during a photocatalytic process can favour the occurrence of a thermal activation mechanism [52]. With these precedents in the present study we have carried out several experiments to gain some insights about the photocatalytic mechanism that takes place when using the optimized the RuO_x(10 wt%)@MIL-125(Ti)–NH_2 photocatalyst for the CO_2 methanation process. As it has been shown before, during the photocatalytic CO_2 methanation by RuO_x(10 wt%)@MIL-125(Ti)–NH_2, RuO_x NPs are reduced at least partially to metallic Ru^0 or partially reduced RuO_x NPs as evidenced by PXRD (Fig. 9b) and XPS (Figure S17), respectively. Therefore, in order to evaluate the possible influence of the presence of oxidized or reduced ruthenium NPs within the MIL-125(Ti)–NH_2 photocatalyst on the mechanistic experiments that have been performed both the fresh and used RuO_x(10 wt%)@MIL-125(Ti)–NH_2 photocatalyst have been used.

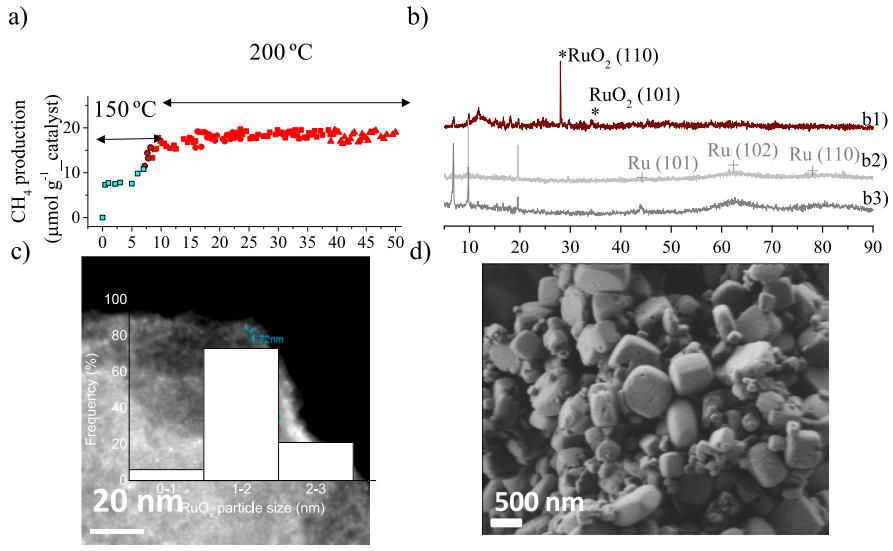

Fig. 9. Photocatalytic CO_2 methanation by RuO_x(10 wt%)@MIL-125(Ti)–NH_2 under continuous flow operation and visible light irradiation ($\lambda > 420$ nm). Reaction conditions: Photocatalyst (50 mg, 0.2 μm, total flow (20 mL/min), mixture of gases (H_2 80% and CO_2 20%), reaction temperature 200 °C, contact time (3 s). b) PXRD of the fresh (b1), 20 h (b2) and 40 h (b3) used photocatalyst c) DF-TEM image and RuO_x particle size distribution of the seven-times used photocatalyst. d) SEM image of the seven-times used photocatalyst.

Initially, the occurrence of a photochemical mechanism was evaluated by performing some specific experiments for this purpose. Firstly, it is worth to comment that RuO_x NPs were supported on MIL-125(Ti)–NH_2 by the photodeposition method that consists of irradiation of MIL-125(Ti)–NH_2 in the presence of water soluble $KRuO_4$ using methanol as sacrificial electron donor. As previously described, the characterization data of the different photocatalysts demonstrated the presence of small RuO_x NPs within the MIL-125(Ti)–NH_2 solid, which indirectly proves that the LMCT process occurred in the MIL-125(Ti)–NH_2 solid under UV–vis irradiation. The photogenerated electrons and holes were responsible for the reduction of $KRuO_4$ to RuO_x and the oxidation of methanol as sacrificial electron donor, respectively. Then, the presence of RuO_x NPs supported on MIL-125(Ti)–NH_2 could favour the LMCT by improving charge separation efficiency. To confirm this hypothesis, the charge transfer energy between MIIL-125(Ti)–NH_2 and ruthenium NPs was studied by means of photoluminescence (PL) spectroscopy [53]. PL measurements were thus carried out for both fresh and used RuO_x(10 wt %)@MIL-125(Ti)–NH_2 samples by using an excitation wavelength of 340 nm, which corresponds to the absorption of the 2-aminoterephthalate present in MIL-125(Ti)–NH_2. Fig. 10a shows that the presence of ruthenium NPs in both the fresh and used RuO_x(10 wt%) @MIL-125(Ti)–NH_2 sample quenches the PL>41% with respect to pristine MIL-125(Ti)–NH_2. This data was interpreted considering that the presence of both metallic Ru and/or RuO_x in the MIL-125(Ti)–NH_2 solid favours the separation of charge carriers during the photocatalysis.

Another common strategy to verify the occurrence of photoinduced charge separation in a material is to measure its photocurrent response [17,53]. For this, a thin film of fresh and used RuO_x(10 wt%)@MIL-125 (Ti)–NH_2 solids were initially deposited onto FTO as transparent conductive electrode, the dark current and photocurrent response of the system were compared at increasing positive voltages. The results are shown in Fig. 10b and Fig. 10b. As can be seen in both figures, illumination of the electrodes at each polarization voltage increased the measured current. In addition, the presence of methanol as electron donor during the photocurrent experiment results in an increase of the photocurrent intensity. This observation agrees with the role of methanol as sacrificial agent that becomes oxidized by giving electrons to the fresh or used RuO_x(10 wt%)@MIL-125(Ti)–NH_2 during the irradiation

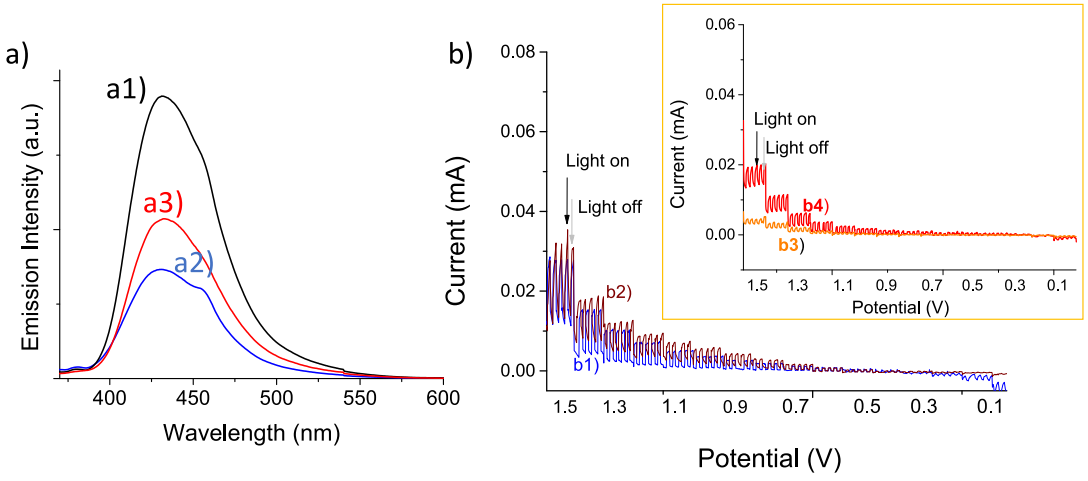

Fig. 10. a) PL emission upon photoexcitation at 340 nm using deaerated acetonitrile suspensions of MIL-125(Ti)–NH_2 (a1), fresh RuO_x(10 wt%)@MIL-125(Ti)–NH_2 (a2) or one-time used RuO_x(10 wt%)@MIL-125(Ti)–NH_2 (a3) in the photocatalytic CO_2 methanation at 200 °C under simulated sunlight irradiation. b) Photocurrent intensity vs. polarization potential measured for the fresh (b1, b2) or used (b3, b4) RuO_x(10 wt%)@MIL-125(Ti)–NH_2 sample supported on a FTO electrode in a deaerated CH_3CN solution of TPAPF6 (0.1 M) in the absence of any additive (b1, b3) or in the presence of MeOH (b2, b4) upon simulated sunlight irradiation (150 W Hg-Xe lamp equipped with a AM 1.5 G filter).

process.

Further measurements were carried out to study the possible reaction mechanism during photocatalytic CO_2 methanation [50]. Electron quenchers can be used in a similar way during photocatalytic CO_2 methanation to underline the process's possible reaction mechanism [17]. In this study nitrobenzene (-0.36 V versus Ag-AgCl) was the electron quencher competing with CO_2 during the photocatalytic reaction with H_2 in the presence of RuO_x(10 wt%)@MIL-125(Ti)–NH_2. The results obtained indicate that the presence of nitrobenzene (80 μL) during the photocatalytic reaction at 200 °C under simulated sunlight irradiation inhibits in large extend the formation of CH_4 (202 μmol g^{-1} at 22 h). In a similar way, the photocatalytic CO_2 reduction was carried out in the absence of H_2 but in the presence of dimethylaniline (40 μL) as sacrificial electron donor and observing the formation of CH_4 (1 mmol g^{-1} at 22 h under simulated sunlight irradiation).

The above experiments indicate that, at least partially, the RuO_x(10 wt%)@MIL-125(Ti)–NH_2 photocatalyst operates under a photochemical mechanism during the photocatalytic CO_2 methanation. Regardless the obtained experimental evidences supporting the photochemical mechanism, the presence Ru^0 and/or RuO_x NPs within the MIL-125(Ti)–NH_2 material would make feasible the simultaneous operation of a thermochemical pathway where the light energy is transformed into local heat in the ruthenium NPs favouring thermal conversion of CO_2 and H_2 into CH_4 [52]. According to previous reports [17] experimental evidences about the occurrence of local heating in a photocatalyst upon irradiation can be obtained by using inorganic quantum dots (QDs) as local thermometer. This method is based on the quenching of the QDs emission intensity as the temperature of the QDs increases. Figure S20 shows that the PL emission of commercial CdSe-ZnS upon excitation at 450 nm decreases as the temperature increases from 25 to 100 °C or upon irradiation with a Xe-Hg lamp (150 W) at constant macroscopic temperature. These observations are in good agreement with previous reports and the possibility of using QDs as local thermometer [17]. Analogous experiments using CdSe-ZnS QDs supported on RuO_x(10 wt%)MIL-125(Ti)–NH_2 also evidence the occurrence of local heating upon irradiation with a Xe-Hg lamp (Figure S21). Furthermore, it should be remembered that a couple of control experiments under optimized photocatalytic reaction conditions in the dark using fresh RuO_x(10 wt%)@MIL-125(Ti)–NH_2 resulted in photocatalytic CO_2 conversion and CH_4 production of about 38% respect to the total activity found under simulated sunlight irradiation. This observation indicates that the RuO_x(10 wt%)@MIL-125(Ti)–NH_2 is able to act as a thermocatalyst, a fact that agrees with previous reports about the good ability of ruthenium NPs as active centers to promote hydrogenation reactions [7].

In order to gain more insights about the occurrence of a dual photo-thermal mechanism during the photocatalytic CO_2 methanation using RuO_x(10 wt%)@MIL-125(Ti)–NH_2, the influence of the light intensity in this process was also investigated [52,54]. As it can be seen in Fig. 11 the photocatalytic CH_4 production increases linearly up to light intensity of 343 mW/cm^2 while higher light intensities results in a quadratic growth of CH_4 production. The quadratic relationship between catalytic activity and light intensity would indicate the operation of a dual photo-thermal methanation mechanism specially at high light fluxes NPs [52,55]. It should be remember that 1 Sun irradiation is defined equal to 100 mW/cm^2. Therefore, for practical applications commercially available solar concentrators could be used to achieve the irradiances and photocatalytic activities shown in Fig. 11.

Overall, these experiments can be interpreted as showing that the reaction pathway for photocatalytic CO_2 methanation by RuO_x(10 wt%)@MIL-125(Ti)–NH_2 takes place via a dual photo-thermal mechanism.

4. Conclusions

The present study has shown the possibility of using the MIL-125(Ti)–NH_2 benchmark MOF supported RuO_x nanoparticles as photocatalyst for solar-driven CO_2 methanation. The samples prepared with the highest amount of RuO_x NPs (10 wt%; 1.48 ± 0.53 nm) supported on MIL-125(Ti)–NH_2 obtained the highest photocatalytic activity for selective CO_2 conversion to CH_4 under simulated sunlight irradiation at 200 °C. The photocatalytic CH_4 production as a function of temperature followed the Arrhenius plot equation and allowed us to estimate an apparent activation energy for this process of 68.8 kJ mol^{-1}. It should be noted that the RuO_x(10 wt%)/MIL-125(Ti)–NH_2 photocatalyst can be reused at least 10 times (220 h) at 200 °C under simulated sunlight irradiation without a significant loss of activity while maintaining its crystallinity and morphology, as revealed by PXRD and SEM measurements, respectively, while some partial MOF decarboxylation occurs. This photocatalyst is also active and stable during photocatalytic CO_2 methanation at 150 or 200 °C under visible light irradiation ($\lambda > 420$ nm) at least for 50 h. A series of experimental results indicate the that the optimized RuO_x(10 wt%)@MIL-125(Ti)–NH_2 operates under a dual photo-thermal reaction mechanism during the photocatalytic CO_2 methanation.

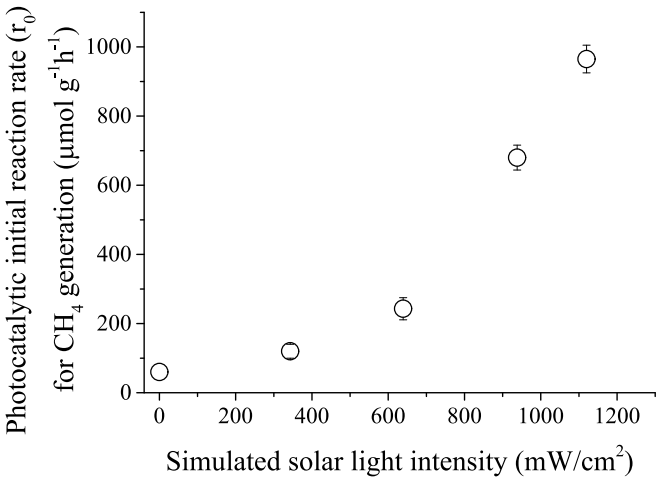

Fig. 11. Photocatalytic initial reaction rate (r_0) for CH_4 generation as a function of the simulated solar light intensity. Reaction conditions: Photocatalyst (15 mg), P_{H2} = 1.05 bar, P_{CO2} = 0.25 bar, reaction temperature (200 °C), simulated sunlight irradiation (Hg-Xe lamp of 150 W equipped with an AM 1.5G type filter and the corresponding transmittance filters that decrease the light intensity).

This work exemplifies the possibility of using MOF-based materials as photocatalysts towards the solar-driven selective CO_2 methanation under a continuous flow operation.

Declaration of Competing Interest

The authors declare that they have no known competing financial interests or personal relationships that could have appeared to influence the work reported in this paper.

Acknowledgements

This work was supported by Ministerio de Ciencia, Innovación y Universidades [2022 project] and Generalitat Valenciana (PROMETEO/2021/038). M. C.-A. also thanks financial support by Generalitat Valenciana (PROMETEO/2021/038) for a postdoctoral contract.

Appendix A. Supplementary data

Supplementary data to this article can be found online at https://doi.org/10.1016/j.cej.2022.136426.

References

[1] W. Wang, M.O. Tadé, Z. Shao, Research progress of perovskite materials in photocatalysis- and photovoltaics-related energy conversion and environmental treatment, Chem. Soc. Rev. 44 (2015) 5371–5408, https://doi.org/10.1039/C5CS00113G.

[2] S. Paraschiv, L.S. Paraschiv, Trends of carbon dioxide (CO_2) emissions from fossil fuels combustion (coal, gas and oil) in the EU member states from 1960 to 2018, Energy Rep. 6 (2020) 237–242, https://doi.org/10.1016/j.egyr.2020.11.116.

[3] R. Shahnazi, Z.D. Shabani, The effects of renewable energy, spatial spillover of CO_2 emissions and economic freedom on CO_2 emissions in the EU, Renew. Energy 169 (2021) 293–307, https://doi.org/10.1016/j.renene.2021.01.016.

[4] P. Friedlingstein, M. O'Sullivan, M.W. Jones, R.M. Andrew, J. Hauck, A. Olsen, G.P. P. Peters, W. Peters, J. Pongratz, S. Sitch, C. Le Quéré, J.G. Canadell, P. Ciais, R. B. Jackson, S. Alin, L.E.O.C. Aragão, A. Arneth, V. Arora, N.R.R. Bates, M. Becker, A. Benoit-Cattin, H.C.C. Bittig, L. Bopp, S. Bultan, N. Chandra, F. Chevallier, L. P. Chini, W. Evans, L. Florentie, P.M. Forster, T. Gasser, M. Gehlen, D. Gilfillan, T. Gkritzalis, L. Gregor, N. Gruber, I. Harris, K. Hartung, V. Haverd, R.A. Hughton, T. Ilyina, A.K. Jain, E. Joetzjer, K. Kadono, E. Kato, V. Kitidis, J.I. Korsbakken, P. Landschützer, N. Lefèvre, A. Lenton, S. Lienert, Z. Liu, D. Lombardozzi, G. Marland, N. Metzl, D.R. Munro, J.E.M.S. Nabel, S.-I. Nakaoka, Y. Niwa, K. O'Brien, T. Ono, P.I. Palmer, D. Pierrot, B. Poulter, L. Resplandy, E. Robertson, C. Rödenbeck, J. Schwinger, R. Séférian, I. Skjelvan, A.J.P. Smith, A.J. Sutton, T. Tanhua, P. Tans, H. Tian, B. Tilbrook, G. van der Werf, N. Vuichard, A.P. Walker, R. Wanninkhof, A.J. Watson, D. Willis, A.J. Wiltshire, W. Yuan, X. Yue, S. Zaehle, Global carbon budget, Earth Syst. Sci. Data 12 (2020) 3269–3340, https://doi.org/10.5194/essd-12-3269-2020.

[5] C.F. Shih, T. Zhang, J. Li, C. Bai, Powering the future with liquid sunshine, Joule 2 (2018) 1925–1949, https://doi.org/10.1016/j.joule.2018.08.016.

[6] S. Hamels, E. Himpe, J. Laverge, M. Delghust, K.V. den Brande, A. Janssens, J. Albrechta, The use of primary energy factors and CO_2 intensities for electricity in the European context - A systematic methodological review and critical evaluation of the contemporary literature, Renew. Sustain. Energy Rev. 146 (2021), 111182, https://doi.org/10.1016/j.rser.2021.111182.

[7] M. Younas, L.L. Loong Kong, M.J.K. Bashir, H. Nadeem, A. Shehzad, S. Sethupathi, Recent advancements, fundamental challenges, and opportunities in catalytic methanation of CO_2, Energ. Fuels 30 (2016) 8815–8831, https://doi.org/10.1021/acs.energyfuels.6b01723.

[8] A. Fujishima, K. Honda, Electrochemical photolysis of water at a semiconductor electrode, Nature 238 (1972) 37–38, https://doi.org/10.1038/238037a0.

[9] K.R. Thampi, J. Kiwi, M. Graetzel, Methanation and photo-methanation of carbon-dioxide at room-temperature and atmospheric-pressure, Nature 327 (1987) 506–508, https://doi.org/10.1038/327506a0.

[10] P.G. O'Brien, K.K. Ghuman, A.A. Jelle, A. Sandhel, T.E. Wood, J.Y.Y. Loh, J. Jia, D. Perovic, C.V. Veer Singh, N.P. Kherani, C.A. Mims, G.A. Ozin, Enhanced photothermal reduction of gaseous CO_2 over silicon photonic crystal supported ruthenium at ambient temperature, Energy Environ. Sci. 11 (2018) 3443–3451, https://doi.org/10.1039/C8EE02347F.

[11] A.A. Jelle, K.K. Ghuman, P.G. O'Brien, M. Hmadeh, A. Sandhel, D.D. Perovic, C. V. Singh, C.A. Mims, G.A. Ozin, Highly efficient ambient temperature CO_2 photomethanation catalyzed by nanostructured RuO_2 on silicon photonic crystal support, Adv. Energy Mater. 8 (2018) 1702277, https://doi.org/10.1002/aenm.201702277.

[12] D. Mateo, J. Albero, H. García, Photoassisted methanation using Cu_2O nanoparticles supported on graphene as a photocatalyst, Energy Environ. Sci. 10 (2017) 2392–2400, https://doi.org/10.1039/C7EE02287E.

[13] D. Mateo, J. Albero, H. García, Graphene supported NiO/Ni nanoparticles as efficient photocatalyst for gas phase CO_2 reduction with hydrogen, Appl. Catal. B.-Environ. 224 (2018) 563–571, https://doi.org/10.1016/j.apcatb.2017.10.071.

[14] A. Anouar, R. García-Aboal, P. Atienzar, A. Franconetti, N. Katir, A. El Kadib, A. Primo, H. Garcia, Remarkable activity of 002 facet of ruthenium nanoparticles grown on graphene films on the photocatalytic CO_2 methanation, Adv. Sustainable Syst. (2022) 2100487, https://doi.org/10.1002/adsu.202100487.

[15] J. Barrio, D. Mateo, J. Albero, H. García, M. Shalom, A heterogeneous carbon nitride–nickel photocatalyst for efficient low-temperature CO_2 methanation, Adv. Energy Mater. 9 (2019) 1902738, https://doi.org/10.1002/aenm.201902738.

[16] D. Mateo, J. Albero, H. Garcıa, Titanium-perovskite-supported RuO_2 nanoparticles for photocatalytic CO_2 methanation, Joule 3 (2019) 1949–1962, https://doi.org/10.1016/j.joule.2019.06.001.

[17] S. Wang, M. Cabrero-Antonino, S. Navalón, C.-C. Cao, A. Tissot, I. Dovgaliuk, J. Marrot, C. Martineau-Corcos, L. Yu, H. Wang, W. Shepard, H. García, C. Serre, A robust titanium isophthalate metal-organic framework for visible-light photocatalytic CO_2 methanation, Chemistry 6 (12) (2020) 3409–3427.

[18] M. Cabrero-Antonino, S. Remiro-Buenamañana, M. Souto, A.A. García-Valdivia, D. Choquesillo-Lazarte, S. Navalón, A. Rodríguez-Diéguez, G. Mínguez-Espallargas, H. García, Design of cost-efficient and photocatalytically active Zn-based MOFs decorated with Cu_2O nanoparticles for CO_2 methanation, Chem. Commun. 55 (2019) 10932–10935, https://doi.org/10.1039/C9CC04446A.

[19] I.S. Khan, D. Mateo, G. Shterk, T. Shoinkhorova, D. Poloneeva, L. Garzón-Tovar, J. Gascon, An efficient metal–organic framework-derived nickel catalyst for the light driven methanation of CO_2, Angew. Chem. Int. Ed. 60 (2021) 26476–26482, https://doi.org/10.1002/anie.202111854.

[20] D. Mateo, P. Maity, G. Shterk, O.F. Mohammed, J. Gascon, Tunable selectivity in CO2 photo-thermal reduction by perovskite-supported Pd nanoparticles, ChemSusChem 14 (2021) 5525–5533, https://doi.org/10.1002/cssc.202101950.

[21] G. Férey, C. Mellot-Draznieks, C. Serre, F. Millange, J. Dutour, S. Surblé, I. Margiolaki, A chromium terephthalate-based solid with unusually large pore volumes and surface area, Science 23 (2005) 2040–2042, https://doi.org/10.1126/science.1116275.

[22] H. Furukawa, K.E. Cordova, M. O'Keeffe, O.M. Yaghi, The chemistry and applications of metal-organic frameworks, Science 341 (2013) 1230444, https://doi.org/10.1126/science.1230444.

[23] S. Kitagawa, R. Kitaura, S.-I. Noro, Functional porous coordination polymers, Angew. Chem. Int. Ed. 43 (2004) 2334–2375, https://doi.org/10.1126/science.1230444.

[24] A. Dhakshinamoorthy, A.M. Asiri, H. García, Metal-organic framework (MOF) compounds: photocatalysts for redox reactions and solar fuel production, Angew. Chem. Int. Ed. 55 (2016) 5414–5445, https://doi.org/10.1002/anie.201505581.

[25] A. Dhakshinamoorthy, Z. Li, H. Garcia, Catalysis and photocatalysis by metal organic frameworks, Chem. Soc. Rev. 47 (2018) 8134–8172, https://doi.org/10.1039/C8CS00256H.

[26] X. Chen, X. Peng, L. Jiang, X. Yuan, H. Yub, H. Wang, J. Zhang, Q. Qi Xia, Recent advances in titanium metal–organic frameworks and their derived materials: features, fabrication, and photocatalytic applications, Chem. Eng. J. 395 (2020), 125080, https://doi.org/10.1016/j.cej.2020.125080.

[27] Y. Yan, C. Li, Y. Wu, J. Gao, Q. Zhang, From isolated Ti-oxo clusters to infinite Ti-oxo chains and sheets: recent advances in photoactive Ti-based MOFs, J. Mater. Chem. A 8 (2020) 15245–15270, https://doi.org/10.1039/D0TA03749D.

[28] J. Zhu, P.-Z. Li, W. Guo, Y. Zhao, R. Zou, Titanium-based metal–organic frameworks for photocatalytic applications, Coord. Chem. Rev. 359 (2018) 80–101, https://doi.org/10.1016/j.ccr.2017.12.013.

[29] P. Salcedo-Abraira, A. Babaryk, E. Montero-Lanzuela, O.R. Contreras-Almenor, M. Cabrero-Antonino, E. Svensson Grape, T. Willhammar, S. Navalón, E. Elkäim, H. García, P. Horcajada, A novel porous Ti-squarate as efficient photocatalyst in the overall water splitting reaction under simulated sunlight irradiation, Adv. Mater. 33 (2021) 2106627, https://doi.org/10.1002/adma.202106627.

[30] J. Wang, A.S. Cherevan, C. Hannecart, S. Naghdi, S.P. Nandan, T. Gupta, D. Edera, Ti-based MOFs: new insights on the impact of ligand composition and hole scavengers on stability, charge separation and photocatalytic hydrogen evolution, Appl. Catal. B.-Environ. 283 (2021), 119626, https://doi.org/10.1016/j.apcatb.2020.119626.

[31] M. Cabrero-Antonino, J. Albero, C. García-Vallés, M. Álvaro, S. Navalón, H. García, Plasma-induced defects enhance the visible-light photocatalytic activity of MIL-125(Ti)-NH2 for overall water splitting, Chem. Eur. J. 26 (2020) 15682–15689, https://doi.org/10.1002/chem.202003763.

[32] M.A. Nasalevich, C.H. Hendon, J.G. Santaclara, K. Svane, B. van der Linden, S. L. Veber, M. Fedin, A.J. Houtepen, M.A. van der Veen, F. Kapteijn, A. Walsh, J. Gascon, Electronic origins of photocatalytic activity in d0 metal organic frameworks, Sci. Rep. 6 (2016) 23676, https://doi.org/10.1038/srep23676.

[33] M.A. Nasalevich, R. Becker, E.V. Ramos-Fernandez, S. Castellanos, S.L. Veber, M. V. Fedin, F. Kapteijn, J.N.H. Reek, J.I. van der Vlugt, J. Gascon, Co@NH2-MIL-125 (Ti): cobaloxime-derived metal–organic framework-based composite for lightdriven H2 production, Energy Environ. Sci. 8 (2015) 364–375, https://doi.org/10.1039/C4EE02853H.

[34] S. Remiro-Buenamañana, M. Cabrero-Antonino, M. Martínez-Guanter, M. Álvaro, S. Navalón, H. García, Influence of co-catalysts on the photocatalytic activity of MIL-125(Ti)-NH2 in the overall water splitting, Appl. Catal. B. Environ. (2019) 677–684, https://doi.org/10.1016/j.apcatb.2019.05.027.

[35] M.A. Moreira, J.C. Santos, A.F.P. Ferreira, J.M. Loureiro, F. Ragon, P. Horcajada, P. G. Yot, C. Serre, A.E. Rodrigues, Effect of ethylbenzene in p-xylene selectivity of the porous titanium amino terephthalate MIL-125(Ti)_NH2, Microporous Mesoporous Mater. 158 (2012) 229–234, https://doi.org/10.1016/j.micromeso.2012.03.039.

[36] M.A. Nasalevich, M.G. Goesten, T.J. Savenije, F. Kapteijn, J. Gascon, Enhancing optical absorption of metal–organic frameworks for improved visible light photocatalysis, Chem. Commun. 49 (2013) 10575–10577, https://doi.org/10.1039/C3CC46398B.

[37] Z. Xiao, X. Jiang, B. Li, X. Liu, X. Huang, Y. Zhang, Q. Ren, J. Luo, Z. Qin, J. Hu, Hydrous RuO2 nanoparticles as an efficient NIR-light induced photothermal agent for ablation of cancer cells in vitro and in vivo Nanoscale 7 (2015) 11962-11970. 10.1039/C5NR00965K.

[38] T.P.L. Giang, T.N.M. Tran, X.T. Le, Preparation and characterization of titanium dioxide nanotube array supported hydrated ruthenium oxide catalysts, Adv. Nat. Sci.-Nanosci. Nanotechnol. 3 (2012), 015008, https://doi.org/10.1088/2043-6262/3/1/015008.

[39] D.J. Morgan, Resolving ruthenium: XPS studies of common ruthenium materials, Surf. Interface. Anal. 47 (2015) 1072–1079, https://doi.org/10.1002/sia.5852.

[40] K. Wenderich, G. Mul, Mechanism, and applications of photodeposition in photocatalysis: a review, Chem. Rev. 116 (2016) 14587–14619, https://doi.org/10.1021/acs.chemrev.6b00327.

[41] J.Y. Hwang, M.F. El-Kadya, Y. Wang, L. Wang, Y. Shao, K. Marsh, J.M. Ko, R. B. Kaner, Direct preparation and processing of graphene/RuO_2 nanocomposite electrodes for high-performance capacitive energy storage, Nano Energ. 18 (2015) 57–70, https://doi.org/10.1016/j.nanoen.2015.09.009.

[42] S. Navalón, M. Álvaro, A. Dhakshinamoorthy, H. García, Encapsulation of metal nanoparticles within metal-organic frameworks for the reduction of nitro compounds, Molecules 24 (2019) 3050, https://doi.org/10.3390/molecules24173050.

[43] S. Navalón, A. Dhakshinamoorthy, M. Álvaro, H. García, Diamond nanoparticles in heterogeneous catalysis, Chem. Mater. 32 (2020) 4116–4143, https://doi.org/10.1021/acs.chemmater.0c00204.

[44] A. Santiago-Portillo, M. Cabrero-Antonino, M. Álvaro, S. Navalón, H. García, Tuning the microenvironment of gold nanoparticles encapsulated within MIL-101 (Cr) for the selective oxidation of alcohols with O_2: influence of the amino terephthalate linker, Chem. Eur. J. 25 (2019) 9280–9286, https://doi.org/10.3390/nano10010151.
[45] J. Albero, Y. Peng, H. García, Photocatalytic CO_2 reduction to C2+ products, ACS Catal. 10 (2020) 5734–5749, https://doi.org/10.1021/acscatal.0c00478.
[46] S. Bordiga, C. Lamberti, F. Bonino, A. Travertd, F. Thibault-Starzyk, Probing zeolites by vibrational spectroscopies, Chem. Soc. Rev. 44 (2015) 7262–7341, https://doi.org/10.1039/C5CS00396B.
[47] E. López-Maya, N.M. Padial, J. Castells-Gil, C.R.R. Ganivet, A.R. Gaspar, F. G. Cirujano, N. Almora-Barrios, S. Tatay, S. Navalon, C. MartÍ-Gastaldo, Selective implantation of diamines for cooperative catalysis in isoreticular heterometallic titanium–organic frameworks, Angew. Chem. Int. Ed. 60 (2021) 11868–11873, https://doi.org/10.1002/anie.202100176.
[48] A. Adeyemo, G. Hunter, P.K. Dutta, Interaction of CO with hydrous ruthenium oxide and development of a chemoresistive ambient CO sensor, Sensor Actuat B-Chem. 152 (2011) 307–315, https://doi.org/10.1016/j.snb.2010.12.027.
[49] M. Kobayashi, T. Shirasaki, The chemisorption of CO on ruthenium metals and ruthenium-silica catalysts, J. Catal. 28 (1973) 289–295, https://doi.org/10.1016/0021-9517(73)90013-4.
[50] D. Mateo, A. Santiago-Portillo, J. Albero, S. Navalon, M. Alvaro, H. García, Long-term photostability in terephthalate metal–organic frameworks, Angew. Chem. Int. Ed. (2019) 17843–17848, https://doi.org/10.1002/anie.201911600.
[51] J. Zhou, Z. Gao, G. Xiang, T. Zhai, Z. Liu, W. Zhao, X. Liang, L. Wang, Interfacial compatibility critically controls Ru/TiO_2 metal-support interaction modes in CO_2 hydrogenation, Nat. Commun. 327 (2022) 2418, https://doi.org/10.1038/s41467-021-27910-4.
[52] D. Mateo, J.L. Cerrillo, S. Durini, J. Gascon, Fundamentals and applications of photo-thermal catalysis, Chem. Soc. Rev. 50 (2021) 21732210, https://doi.org/10.1039/D0CS00357C.
[53] J.-D. Xiao, Q. Shang, Y. Xiong, Q. Zhang, Y. Luo, S.-H. Yu, H.-L. Jiang, Boosting photocatalytic hydrogen production of a metal–organic framework decorated with platinum nanoparticles: the platinum location matters, Angew. Chem. Int. Ed. 128 (2016) 9535–9539, https://doi.org/10.1002/ange.201603990.
[54] Q. Xiao, Z. Liu, F. Wang, S. Sarina, H. Zhu, Tuning the reduction power of visible-light photocatalysts of gold nanoparticles for selective reduction of nitroaromatics to azoxy-compounds—Tailoring the catalyst support, Appl. Catal. B- Environ 209 (2017) 69–79, https://doi.org/10.1016/j.apcatb.2017.03.002.
[55] P. Christopher, H.L. Xin, A. Marimuthu, S. Linic, Singular characteristics and unique chemical bond activation mechanisms of photocatalytic reactions on plasmonic nanostructures, Nat. Mater. 11 (2012) 1044–1050, https://doi.org/10.1038/nmat3454.